

Research Paper

Numerical Modelling of Post-Ground Subsystem in Road Safety Barrier Crash Tests

Marian KLASZTORNY¹*, Daniel Bronisław NYCZ²), Paweł DZIEWULSKI¹)
Roman GIELETA¹), Michał STANKIEWICZ¹), Karol ZIELONKA³)

¹) *Department of Mechanics and Applied Computer Science*
Faculty of Mechanical Engineering
Military University of Technology

Gen. S. Kaliskiego 2, 00-908 Warsaw, Poland

e-mail: {pawel.dziewulski; roman.gieleta; michal.stankiewicz}@wat.edu.pl

*Corresponding Author e-mail: marian.klasztorny@wat.edu.pl

²) *Institute of Technology*
Jan Grodek State Vocational Academy

Reymonta 6, 38-500 Sanok, Poland

e-mail: dnycz@pwsz-sanok.edu.pl

³) *Automotive Industry Institute*
Jagiellonska 55, 03-301 Warsaw, Poland

e-mail: k.zielonka@pimot.eu

A new analytical algorithm for determining the elastoplastic parameters for soft, medium and hard plastic cohesive soils, corresponding to *MAT_005_SOIL_AND_FOAM material model available LS-Dyna FE code, was formulated. The numerical modelling of the post-soil subsystem, applicable in the modelling of road safety barrier crash tests using this material model of the roadside dehydrated ground, was developed. The methodology was presented on the example of a Sigma-100 steel post partly driven into the soil and subjected to a static flexural-torsional test using a horizontal tensioned rope. The experimental validation of the numerical modelling and simulation was carried out on the testing site at the Automotive Industry Institute, Warsaw, Poland. The simulations were carried out for numerical models with soil solid elements with reduced integration (ELFORM_1) and full integration (ELFORM_2). The simulation results are in the form of graphs of the rope tension vs. displacement of the upper measurement point of the post and in the form of deformation of the post-soil system. It was shown that the validation experiment was carried out on the post embedded in hydrated soft plastic cohesive soil.

Key words: cohesive soil; material modelling; elastoplastic parameters; post-soil system; numerical modelling; experimental validation.

NOTATIONS

- $a_i, i = 1, 2, 3$ – material constants determining plasticity surface of cohesive soil,
 $A, B, C, D, \alpha, \beta$ – indirect variables in analytic transformations,
 c – cohesion,
 E – Young’s modulus for cohesive soil,
 F – stretching force,
 G – shear modulus for cohesive soil,
 J_2 – second invariant of stress deviator,
 p – pressure,
 K – bulk modulus for loading for cohesive soil,
 K_u – bulk modulus for unloading for cohesive soil,
 s – horizontal displacement,
 $s_i, i = 1, 2, 3$ – horizontal displacements at points 1, 2, 3,
 s_{ij} – stress deviator,
 ν – Poisson’s ratio for cohesive soil,
 φ – internal friction angle,
 σ – normal stress,
 σ_1 – vertical pressure,
 σ_3 – horizontal pressure,
 τ – shear stress,
H – hard plastic cohesive soil,
M – medium plastic cohesive soil,
S – soft plastic cohesive soil,
2-D – two-dimensional,
3-D – three-dimensional,
FE – finite element,
FEM – finite element method,
CPU – central processing unit.

1. INTRODUCTION

A typical steel road safety barrier consists of a guiderail, spacers and posts, connected with screws. The posts are embedded in dehydrated roadside soil. The post-soil interaction significantly affects the barrier performance. Therefore, adequate modelling of roadside soil plays an important role in simulation of road safety barrier crash tests.

Two main empirical approaches, respectively based on the static and dynamic tests, were developed to simulate the post-soil interaction. The tests are conducted for a post partly driven into the soil and loaded horizontally at a certain height above the ground level. The static tests are performed under displacement or force controlling [1]. The dynamic tests use a head hitting the post with a big kinetic energy. The head can be a pendulum, a block trailed by a rope, or a block driven unidirectionally by a pneumatic system [2, 3]. The static tests are much

simpler than dynamic tests and allow to identify the elastoplastic parameters of the soil model independently of the soil inertia and damping properties. Statically loaded posts embedded in different roadsides were modelled numerically using the FEM [4, 5].

In the numerical models of road barrier crash tests, the post-soil subsystem was modelled with spring elements whose stiffness depends on the depth [6–10], solid elements [11–13] or by means of spring and solid elements [14]. In this work, numerical modelling of the post-soil interaction in the LS-Dyna system was developed, using solid finite elements for the soil.

Material models available in the LS-Dyna environment to describe soil behaviour can be divided into three groups depending on the possibility of taking into account the damage and strain ratio [15]. The simplest soil model is the *MAT_005_SOIL_AND_FOAM material model which can be used to describe foam and soil materials in the case when their properties are not fully known [16]. For any location of a road safety barrier the elastoplastic properties of the soil cannot be determined accurately. The *MAT_005 model, in which the strength depends on the pressure, is described in [17–19].

Advances in the post-soil interaction for static and dynamic loads are presented in [1]. Experimental studies and numerical modelling were carried out for the SIGMA post. The soil was described using the *MAT_078_SOIL_CONCRETE and *MAT_FHWA_SOIL material models [20]. Differences in the force-displacement graphs in four static experimental tests were noted, justified by differences in soil compaction.

The study presents a new algorithm for calculating the elastoplastic parameters of soft (S), medium (M) and hard (H) plastic cohesive soils as well as a new methodology for numerical modelling of the post-soil system, applicable in the modelling of road safety barrier crash tests. The methodology was developed on a Sigma-100 steel post [21] partly driven into the soil and subjected to a static flexural-torsional test using a horizontal tensioned rope. For the soil, the isotropic material model *MAT_005_SOIL_AND_FOAM, available in LS-Dyna FE code, was applied. The numerical modelling and simulation of the post-soil system was partly validated experimentally.

2. EXPERIMENTAL STATIC POST-SOIL TEST

The subject of experimental investigations is a SIGMA-100 steel post, of a length of 1.90 m, embedded in the cohesive soil of the testing site of the Automotive Industry Institute, Warsaw, Poland. The post was partly driven into the soil to a depth of 1.20 m, at a distance of 0.30 m from the concrete slab edge. Due to intense rainfall a day before the test, the soil was partly hydrated, without the possibility of full dehydration. The irrigation of the soil

on the training ground was an unplanned random situation. The upper visible part of the ground was damp, but not wet. The experimental test conditions were unfavourable from the point of view of the validation of the numerical modelling and simulation of the post-soil system.

The post was subjected to a static flexural-torsional test carried out in July 2017. A thick steel clamp was mounted on the top of the post, to which a head measuring the horizontal rope stretching force was attached. The post was loaded by means of a steel rope hooked to a forklift moving at a quasi-static constant velocity of around 5 cm/s (Fig. 1). This excitation is approximately under displacement controlling. The rope was located horizontally in the direction perpendicular to the concrete slab edge.

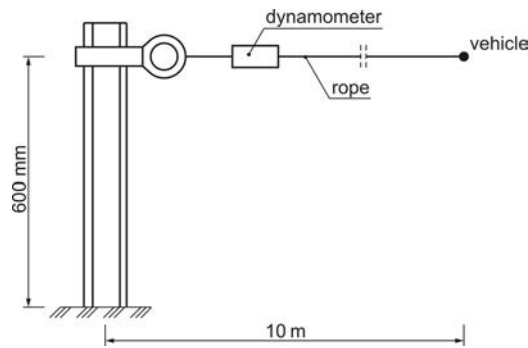


FIG. 1. Diagram of experimental post-soil test.

Figure 2 shows the test station with the apparatus specified in the figure caption. The test was recorded using a Phantom v12 camera (not visible in

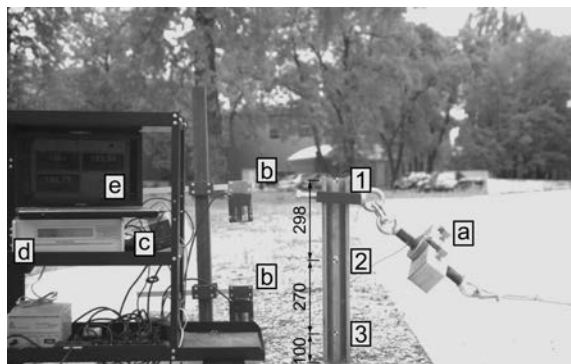


FIG. 2. Test station (general view): a) Rcz force measuring head (range of 100 kN), b) LK-G502 laser displacement sensors (producer Keyence), c) LK-G3001V conditioner for displacement sensors (producer Keyence), d) ESAM Traveller CF strain gauge bridge (producer ESAM GmbH), e) computer with software for signal acquisition; (1)–(3) displacement measurement points using Phantom camera.

Fig. 2), at a sampling frequency of 10^3 Hz. No filtering of the recorded data was used. The displacement measurement points were marked as 1, 2, 3. Control points for displacement measurement of the post by means of laser sensors were at the heights of 125 mm and 515 mm above the ground level. TEMA 3D software was used to process the camera data.

Figure 3 shows the post and soil deformations for selected horizontal displacements of the upper measurement point. Typical soil surface deformation around the post is visible. Figure 4 shows the $F(s)$ curves corresponding to the displacements at points 1, 2, 3. The maximum value of force F is 11.8 kN and corresponds to the displacements $s_1 = 247$ mm, $s_2 = 185$ mm, and $s_3 = 125$ mm. Relatively small resistance and slips before achieving the maximum value of force F confirm partial hydration of the soil.

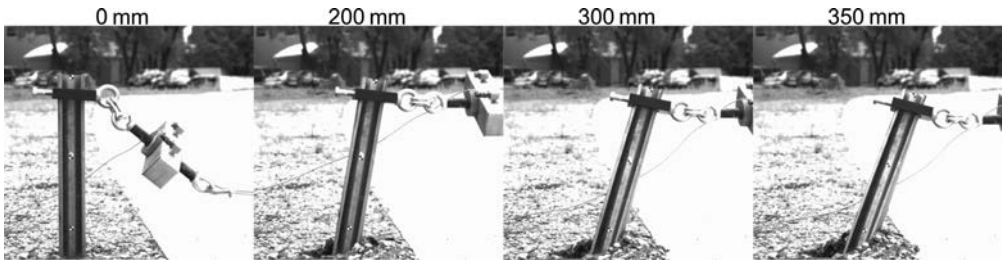


FIG. 3. Experimental deformations of post and soil surface for selected horizontal displacements of point 1.

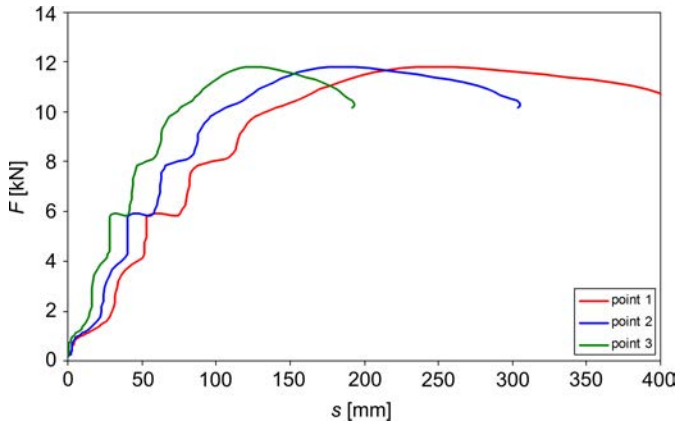


FIG. 4. $F(s)$ curves corresponding to points 1, 2, 3.

The final deformation of the post and soil is shown in Fig. 5. The displacement is smaller than the maximum due to the elastic return after removing the load.

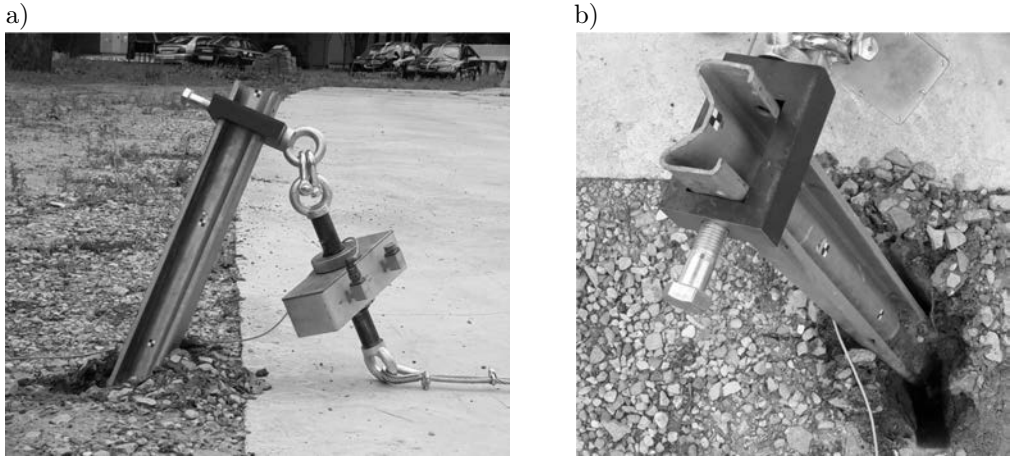


FIG. 5. Final deformation of post and soil after release of rope:
a) side view; b) view from above.

3. NUMERICAL MODELLING OF POST-SOIL SYSTEM

The numerical and material model of the SIGMA-100 post was developed taking into account the Stalprodukt S.A. catalogue data [21]. In the description of the parameters and options of the numerical modelling and simulation, the corresponding labels from the LS-Dyna manuals were used [16, 20].

The soil in the form of a cylinder with a diameter of 1.00 m and a height of 1.52 m was assumed and meshed using 3-D FEs with HEXA and PENTA topologies. The FEs were assigned the formulation ELFORM_1 (8-node solid element described with trilinear shape functions, with 1 integration point) or ELFORM_2 (8-node solid element described with trilinear shape functions, fully integrated, with 8 integration points). The dimensions of the cylinder are consistent with the values recommended by National Crash Analysis Center, USA (<http://www.ncac.gwu.edu/vml/modes.html> (accessed Sept. 18, 2014)). The effect of the slight embedment of the concrete slab (thickness of 0.30 m) into the soil cylinder is omitted.

The SIGMA-100 post was modelled using 2-D shell FEs with QUAD4 topology, which were assigned the formulation ELFORM_2 (Belytschko-Tsay shell element with one integration point in the element midsurface). The clamp was modelled using 3-D FEs with HEXA and PENTA topologies, assigned the formulation ELFORM_1.

Using an additional outer shell for the *MAT_SOIL_AND_FOAM material model is obligatory [16]. 2-D FEs with QUAD3 and TRIA3 topologies were applied for this shell, which were assigned the formulation ELFORM_2 and the material model *MAT_NULL (*MAT_009). For this model, the density,

Young’s modulus and Poisson’s ratio are defined to determine the contact stiffness. The numerical model of the post-soil system is shown in Fig. 6.

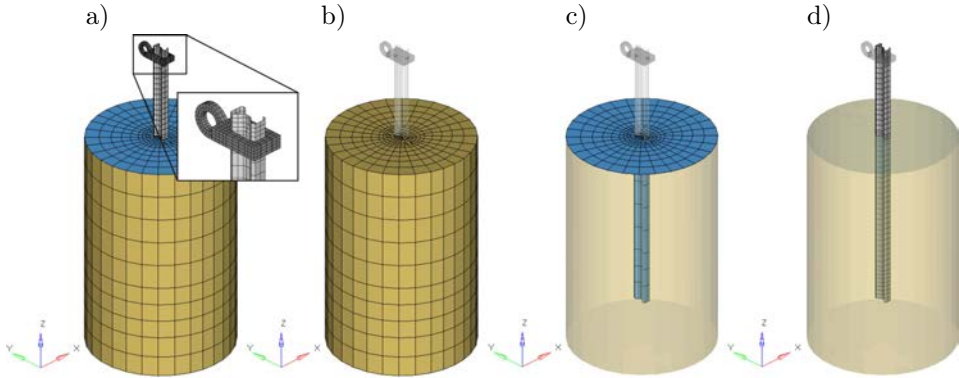


FIG. 6. Post-soil system numerical model: a) full model, b) soil mesh, c) closing shell mesh, d) post mesh.

The isotropic material model `*MAT_PIECEWISE_LINEAR_PLASTICITY` (`* MAT_024`) for steel was adopted. The material constants of steel are listed in Table 1, based on [12]. The parameters `ETAN` and `FAIL` are the simulation parameters (unreal) and have been determined from additional experimental and numerical tests.

Table 1. Steel material constants of SIGMA-100 post corresponding to `*MAT_024` material model.

Parameter [20]	Description	Unit	Value [12]
RO	density	T/mm ³	7.85 · 10 ⁻⁹
E	Young’s modulus	MPa	210 000
PR	Poisson’s ratio	–	0.30
SIGY	yield strength	MPa	320
ETAN	tangent modulus	MPa	900
FAIL	ultimate plastic strain (FE erosion)	–	0.70

The soil is represented by the `*MAT_SOIL_AND_FOAM` (`MAT_005`) model described in Sec. 4. The steel clamp is described by the `*MAT_RIGID` material model (`*MAT_020`). Physical damping with a damping factor of 0.10 in the soil and 0.03 in the post are taken into account [12].

Between the post and the closing shell, the contact model `*CONTACT_AUTOMATIC_SINGLE_SURFACE` was defined with a friction coefficient of 0.30 [12]. The `*CONTACT_AUTOMATIC_SINGLE_SURFACE` contact type, recommended for crash test simulations, is the most widely used contact option

in LS-DYNA. With this type, the slave surface is typically defined as a list of selected parts. No master surface is defined. The contact is considered between all the parts in the slave list, including self-contact of each part. To determine the contact forces, Penalty Method is used. This method consists of placing normal interface springs between all penetrating nodes and the contact surface. The spring stiffness matrix is assembled into the global stiffness matrix of the system. The Standard Penalty Formulation of the penalty algorithm was chosen. In this formulation, the interface stiffness is chosen to be approximately the same order of magnitude as the stiffness of the interface element normal to the interface. The convergence of the simulation is protected by respective scaling up the stiffness and scaling down the time step size. Friction in LS-Dyna FE code is based on a Coulomb formulation [16].

The internal contact model `*CONTACT_INTERIOR` was assigned to the soil in order to eliminate the effect of negative volume. The external surface and the lower base of the soil cylinder were fully fixed. Displacement-controlled excitation was implemented in a single node of the clamp lug (Fig. 7). The Flanagan-Belytschko stiffness hourglass (HG) control procedure was defined globally, with a coefficient of 0.03 [22].

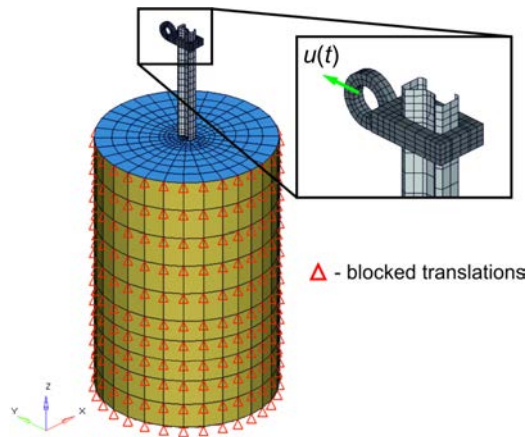


FIG. 7. Boundary conditions in post-soil numerical model.

4. DESCRIPTION AND ANALYSIS OF `*MAT_005_SOIL_AND_FOAM` MATERIAL MODEL

The `*MAT_005_SOIL_AND_FOAM` model for soil requires declaration of a shear modulus, bulk modulus for unloading, three yield function constants, pressure cut-off for tensile fracture and a pressure vs. volumetric strain curve (up to 10 points). The parameters of the model are listed and described in Table 2.

Table 2. *MAT_005_SOIL_AND_FOAM material model parameters (based on [16, 17, 20]).

Parameter	Name	Description	Identification test
RO	Mass density	Mass density (mass/unit volume)	–
G	Shear modulus	Elastic shear modulus, i.e. the slope of the shear stress vs. shear strain curve. It can be calculated based on Young’s modulus and Poisson’s ratio from a uniaxial strain test.	Uniaxial strain test
BULK	Bulk modulus for unloading used for VCR = 0.0	Bulk modulus for unloading, i.e. the slope of the mean stress vs. strain curve when the pressure is reduced (unloaded) from a higher pressure load. It can also be obtained from uniaxial strain unloading.	Hydrostatic compression
A0	Yield function constant for plastic yield function	a_0 is a quadratic fit coefficient. In a J_2 vs. p (second invariant of stress difference vs. pressure) graph, a_0 represents the intersection of the quadratic fit of the shear failure envelope and the J_2 axis. The J_2 vs. p graph is derived from the stress difference vs. normal stress.	Triaxial compression
A1	Yield function constant for plastic yield function	a_1 is a quadratic fit coefficient. It is the initial slope coefficient of the quadratic fit of the shear failure envelope.	Triaxial compression
A2	Yield function constant for plastic yield function	a_2 is a quadratic fit coefficient. It is the curvature coefficient of the quadratic fit of the shear failure envelope.	Triaxial compression
PC	Pressure cut-off for tension fracture (<0)	Pressure cut-off is the maximum tension stress allowed, representing tensile fracture. It is the mean stress intercept of the shear failure envelope.	Triaxial compression
VCR	Volumetric crushing option: 0.0 = on 1.0 = loading and unloading path are the same	VCR = 0 turns on volumetric crushing, defined by the 10 points on the pressure-volumetric strain curve. VCR = 1 turns off. The pressure-volumetric strain curve defines the material deformation at 10 pressures.	–
EPS $_i$, P $_i$	$i = 1-10$ Volumetric strain values (natural logarithmic values); pressure corresponding to volumetric strain values	The pressure-volumetric strain curve. At zero loading there is zero volume change. EPS is the natural logarithmic volumetric strain = $\ln(1 - \epsilon_{vol})$, where $\epsilon_{vol} = (\text{initial volume} - \text{current volume})/\text{initial volume}$.	Uniaxial strain test

The plasticity surface of model *MAT_005 is determined by the function [20]:

$$(4.1) \quad J_2 = \frac{1}{2} s_{ij} s_{ij} = a_0 + a_1 p + a_2 p^2,$$

where J_2 – the second invariant of the stress deviator, p – pressure (positive in compression), a_0, a_1, a_2 – material constants, s_{ij} – stress deviator.

Typical roadsides are made of cohesive soils. The mean values of Young's modulus E , shear modulus G and Poisson's ratio ν for the S, M, and H soils were determined based on the variability intervals given in [23] and are listed in Table 3. Based on the formula

$$(4.2) \quad K = \frac{E}{3(1-2\nu)}$$

and Table 3, the bulk modules for loading were determined and listed in Table 4. The bulk modules for unloading were calculated based on [17] and Eq. (4.2), from the formula $K_u = 3K$, and listed in Table 4.

Table 3. Ranges and average values of elastic constants E, G, ν for cohesive soils (based on [23]).

Soil code	E [MPa]		G [MPa]		ν	
	Range	Average	Range	Average	Range	Average
S	1–15	8	0.5–5	2.75	0.35–0.40	0.375
M	15–30	22.5	5–15	10	0.30–0.35	0.325
H	30–100	65	15–40	27.5	0.20–0.30	0.250

Table 4. Bulk modules for loading and for unloading for cohesive soils.

Soil code	K [MPa]	K_u [MPa]
S	10.7	32.1
M	21.4	64.2
H	43.3	129.9

The Mohr-Coulomb theory is adequate for the shear test of cohesive soil, which is represented in Fig. 8, where [24, 25]: c – cohesion [MPa], φ – internal friction angle [°], σ_1 – vertical pressure (principal normal stress) on a cylindrical soil sample in the triaxial compression test [MPa], σ_3 – horizontal stress (wall pressure on the soil sample) in the triaxial compression test [MPa]. Stresses $\sigma_1 \sigma_3$ are positive in compression. The shear stress is

$$(4.3) \quad \tau = c + \sigma \tan \varphi.$$

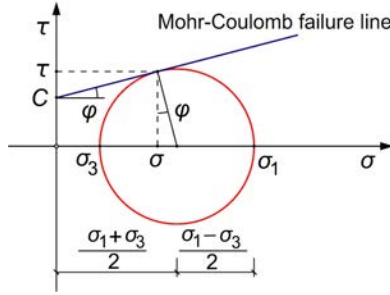


FIG. 8. Mohr-Coulomb theory for cohesive soil.

The hydrostatic pressure is

$$(4.4) \quad p = \frac{1}{3} (\sigma_1 + 2\sigma_3).$$

Going to the shear test, from Eq. (4.3) and Fig. 8 one obtains:

$$(4.5) \quad \tau = \frac{\sigma_1 - \sigma_3}{2} \cos \varphi, \quad \sigma = \frac{\sigma_1 + \sigma_3}{2} - \frac{\sigma_1 - \sigma_3}{2} \sin \varphi.$$

Classic relationships in mechanics of cohesive soils have the form [25]

$$(4.6) \quad \begin{aligned} \sigma_1 &= \sigma_3 \tan^2 \left(45^\circ + \frac{\varphi}{2} \right) + 2c \tan \left(45^\circ + \frac{\varphi}{2} \right), \\ \sigma_3 &= \sigma_1 \tan^2 \left(45^\circ - \frac{\varphi}{2} \right) - 2c \tan \left(45^\circ - \frac{\varphi}{2} \right). \end{aligned}$$

Based on Eqs (4.1) and (4.4)–(4.6), for the *MAT_005 model and the triaxial compression test one obtains:

$$(4.7) \quad \begin{aligned} J_2 &= \frac{1}{3} (\sigma_1 - \sigma_3)^2, \\ \sigma_1 - \sigma_3 &= \sigma_1 - \sigma_1 \tan^2 \left(45^\circ - \frac{\varphi}{2} \right) + 2c \tan \left(45^\circ - \frac{\varphi}{2} \right) = C\sigma_1 + D, \\ C &= 1 - \tan^2 \left(45^\circ - \frac{\varphi}{2} \right), \\ D &= 2c \tan \left(45^\circ - \frac{\varphi}{2} \right), \\ p &= \frac{1}{3} \sigma_1 + \frac{2}{3} \sigma_1 \tan^2 \left(45^\circ - \frac{\varphi}{2} \right) - \frac{4}{3} c \tan \left(45^\circ - \frac{\varphi}{2} \right) = A\sigma_1 - B, \\ A &= \frac{1}{3} + \frac{2}{3} \tan^2 \left(45^\circ - \frac{\varphi}{2} \right), \\ B &= \frac{4}{3} c \tan \left(45^\circ - \frac{\varphi}{2} \right). \end{aligned}$$

From Eqs (4.7) the following results are obtained:

$$\begin{aligned}
 \sigma_1 &= \frac{p+B}{A}, \\
 \sigma_1 - \sigma_3 &= C\sigma_1 + D = C\frac{p+B}{A} + D = \alpha p + \beta, \\
 \alpha &= \frac{C}{A}, \\
 \beta &= \frac{C}{A}B + D \text{ [MPa]}, \\
 J_2 &= \frac{1}{3}(\alpha p + \beta)^2.
 \end{aligned}
 \tag{4.8}$$

Comparing Eqs (4.1) and (4.8)₅, one obtains analytical formulae

$$a_0 = \frac{1}{3}\beta^2 \text{ [MPa}^2\text{]}, \quad a_1 = \frac{2}{3}\alpha\beta \text{ [MPa]}, \quad a_2 = \frac{1}{3}\alpha^2.
 \tag{4.9}$$

The variability ranges and average values of cohesion c and the internal friction angle φ are presented in Table 5 on the basis of [24]. Table 6 presents the parameter values corresponding to the average cohesion and internal friction values (Table 5), calculated according to Eqs (4.7)_{3,4,6,7}, (4.8)_{3,4}, (4.9). Figures 9, 10 show curves $J_2(p)$ and $(\sigma_1 - \sigma_3)(p)$ corresponding to the values listed in Table 6.

Table 5. Variability ranges and average values of cohesion and internal friction angle of cohesive soils (based on [24]).

Soil code	c [MPa]		φ [°]	
	Range	Average	Range	Average
S	0.006–0.035	0.020	3–16	10
M	0.012–0.045	0.028	6–20	13
H	0.020–0.060	0.040	10–25	17

Table 6. Values of parameters a_0 , a_1 , a_2 calculated for average values of cohesion and internal friction angle of cohesive soils.

Soil code	a_0 [MPa ²]	a_1 [MPa]	a_2
S	$5.828 \cdot 10^{-4}$	$1.028 \cdot 10^{-2}$	$4.530 \cdot 10^{-2}$
M	$1.160 \cdot 10^{-3}$	$1.913 \cdot 10^{-2}$	$7.885 \cdot 10^{-2}$
H	$2.395 \cdot 10^{-3}$	$3.661 \cdot 10^{-2}$	$1.399 \cdot 10^{-1}$

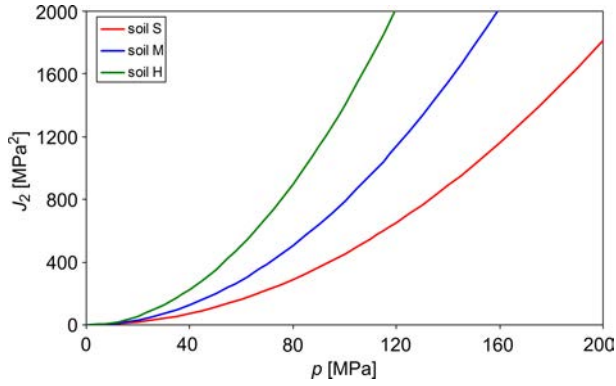


FIG. 9. Curves $J_2(p)$ corresponding to soils S, M, H with parameters a_0, a_1, a_2 taken form Table 6.

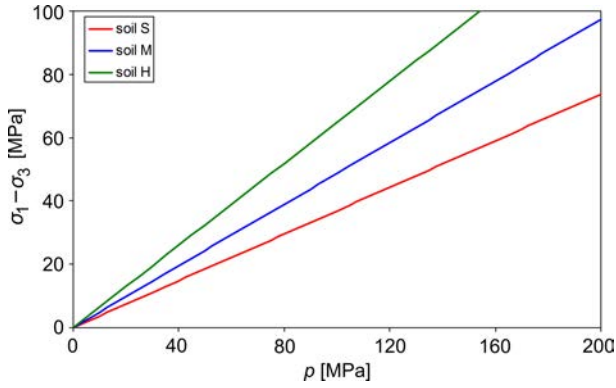


FIG. 10. Curves $(\sigma_1 - \sigma_3)(p)$ corresponding to soils S, M, H with parameters a_0, a_1, a_2 taken from Table 6.

Table 7. *MAT_005_SOIL_AND_FOAM material model parameter values for S, M and H soils, adopted in simulations.

Parameter [20]	Unit	S	M	H
RO	T/mm ³	$2.1 \cdot 10^{-9}$	$2.1 \cdot 10^{-9}$	$2.1 \cdot 10^{-9}$
G	MPa	2.75	10	27.5
BULK	MPa	32.1	64.2	129.9
A0	MPa ²	$5.828 \cdot 10^{-4}$	$1.160 \cdot 10^{-3}$	$2.395 \cdot 10^{-3}$
A1	MPa	$1.028 \cdot 10^{-2}$	$1.913 \cdot 10^{-2}$	$3.661 \cdot 10^{-2}$
A2	–	$4.530 \cdot 10^{-2}$	$7.885 \cdot 10^{-2}$	$1.399 \cdot 10^{-1}$
PC	MPa	–2	–2	–2
EPS _i , P _i	–	–	–	–
K	MPa	10.7	21.4	43.4

Summing up the results collected in Tables 3, 4 and 6, the *MAT_005_SOIL_AND_FOAM material model parameter values for S, M and H soils in a compatible system of units (N, mm, MPa, tone (T)), are listed in Table 7. Parameters RO, PC are taken from [17].

5. SIMULATION RESULTS AND ANALYSIS

5.1. Solid elements with reduced integration

The following previous notation is used: F – rope tension force, s_1 – horizontal displacement of the upper measurement point on the post. Figure 11 shows the $F(s_1)$ simulation curves corresponding to the use of FEs with reduced integration (formulation ELFORM_1, IHQ = 6, QM = 0.03), for cohesive soils S, M, and H, against the background of the experimental curve. The Belytschko-Bindeman anti-hourglass stiffness procedure was adopted (IHQ=6, *assumed strain, co-rotational stiffness formulation*) [16, 22]. The hourglass parameter value QM=0.03 was justified in further considerations.

The simulations were performed using an LS-Dyna v.971 solver (explicit procedure). The velocity of horizontal rope displacement was increased to $v = 210$ cm/s to reduce the CPU time. The speed of 210 cm/s is a low dynamic velocity, causing some oscillations in the dynamic response of the post-soil system. In order to verify the dynamic effects at this speed, the simulations were also carried out for the quasi-static speed of $v = 5$ cm/s applied in the experiment. The results presented in Fig. 11 show that curves corresponding to the speed of 210 cm/s can be used to validate the modelling and simulation.

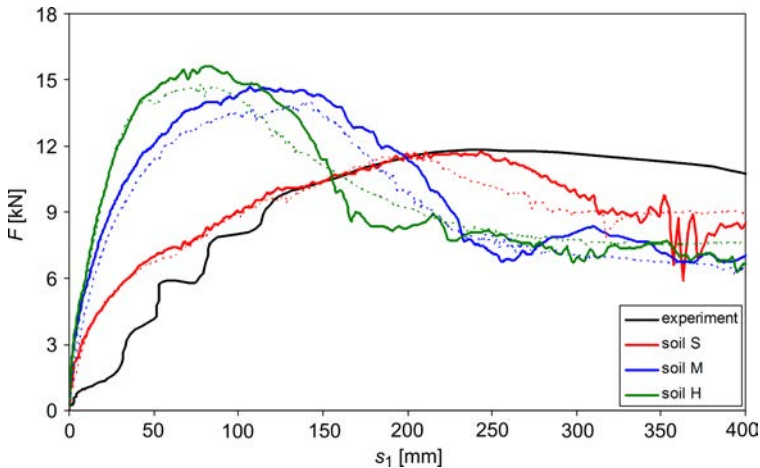


FIG. 11. $F(s_1)$ curves for S, M and H soils, against background of experimental curve (reduced integration): $v = 210$ cm/s (solid lines); $v = 5$ cm/s (dotted lines).

Table 8 lists the maximum values of force F and the corresponding displacements s_1 . The relative difference in the value for soil S in relation to the experimental result is given in parentheses.

Table 8. Maximum values of force F and corresponding displacements s_1 for soil finite elements with reduced integration.

Soil	F [kN]	s_1 [mm]
Experiment	11.8	247
S	12.1 (2.5%)	247 (0%)
M	14.1	110
H	15.6	84

The following conclusions arise from Fig. 11 and Table 8:

- The cohesive soil in the experiment is close to hydrated soil S.
- The $F(s_1)$ simulation curve for soil S is fairly well in line with the experimental curve.
- The M and H soils induce torsion of the post in the contact zone with the soil surface. Torsion of the post causes a substantial drop in force F .

Figure 12 compares the internal energy and hourglass energy for the S soil test. The condition that the hourglass energy should be less than 10% of the internal energy is met [22].

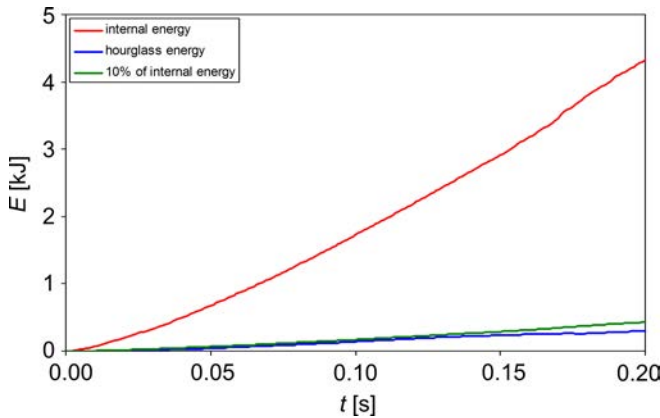


FIG. 12. Comparison of internal energy and hourglass energy for soil S.

The *default* value of the hourglass parameter QM is 0.10 [20]. In the case of modelling soft materials, reducing the value of the QM parameter to avoid stiffening of the system is recommended [22]. Figure 13 shows the impact of the QM parameter on the $F(s_1)$ curve course for soil S. The best compatibility of the simulation and the experiment is obtained for $QM = 0.03$.

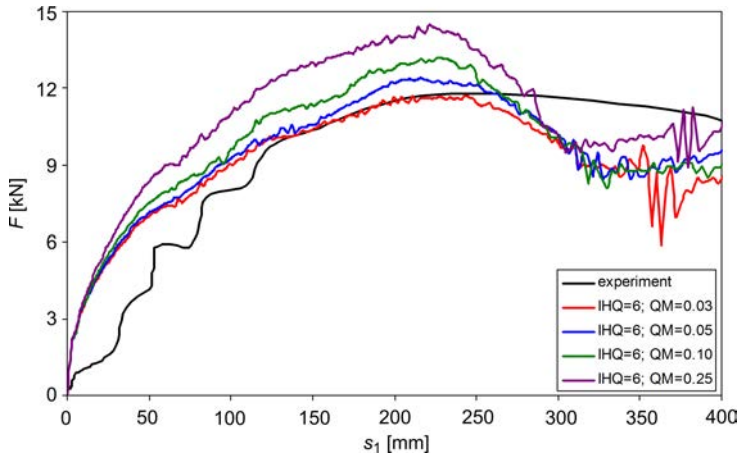


FIG. 13. Comparison of $F(s_1)$ curve for selected values of QM parameter for soil S.

Figure 14 shows the deformation of the post in soils S, M, and H every 100 mm of displacement-controlled excitation. In the case of the H and M soils, there is

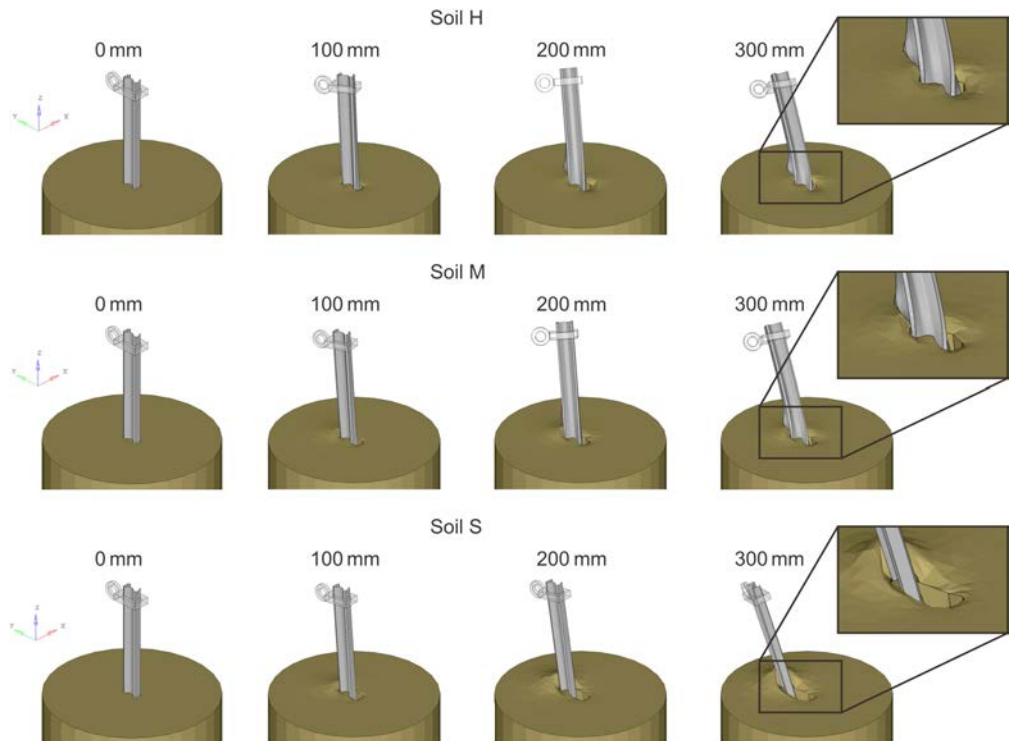


FIG. 14. Deformation of post-soil system every 100 mm of s_1 displacement for H, M, and S soils.

a local loss of stability in the post zone near the soil surface, which results in torsion of the post opposite to the torsion observed during the experimental test. For soil S, much greater deformation of the soil in front of the post is visible. The simulated torsion of the post is consistent with the experimental test. The twisting of the post results from:

- 1) load eccentricity (at the beginning of the process, the rope is perpendicular to the symmetry plane of the post) with respect to the shear centre of the “sigma” monosymmetric cross section,
- 2) rotation of the clamp with dimensions significantly larger than the cross-section of the post,
- 3) post-soil interaction.

Figures 15–17 show the effective stress contour maps according to the Mises-Hencky hypothesis for the deformed SIGMA-100 post (yield point $R_e = 320$ MPa), with displacement $s_1 = 300$ mm (tense rope). The maximum value of effective stress in the SIGMA-100 post for soil S is 385 MPa. After exceeding R_e , steel became locally plasticized. In the case of increasing deformations in the plastic hinge, the effective stresses in the reinforcing zone exceed the yield point.

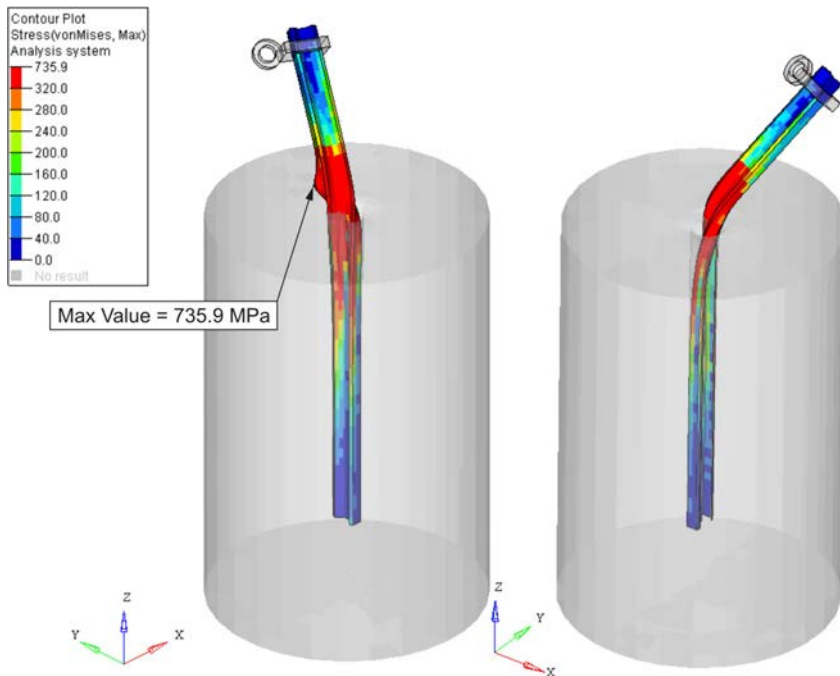


FIG. 15. Effective stress contour map for deformed SIGMA-100 post embedded in soil H, with displacement $s_1 = 300$ mm.

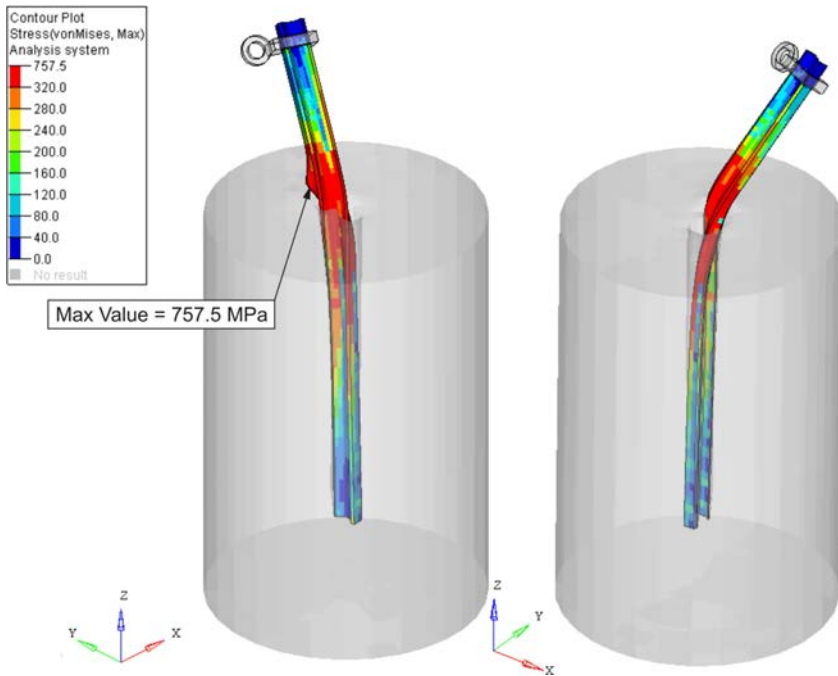


FIG. 16. Effective stress contour map for deformed SIGMA-100 post embedded in soil M, with displacement $s_1 = 300$ mm.

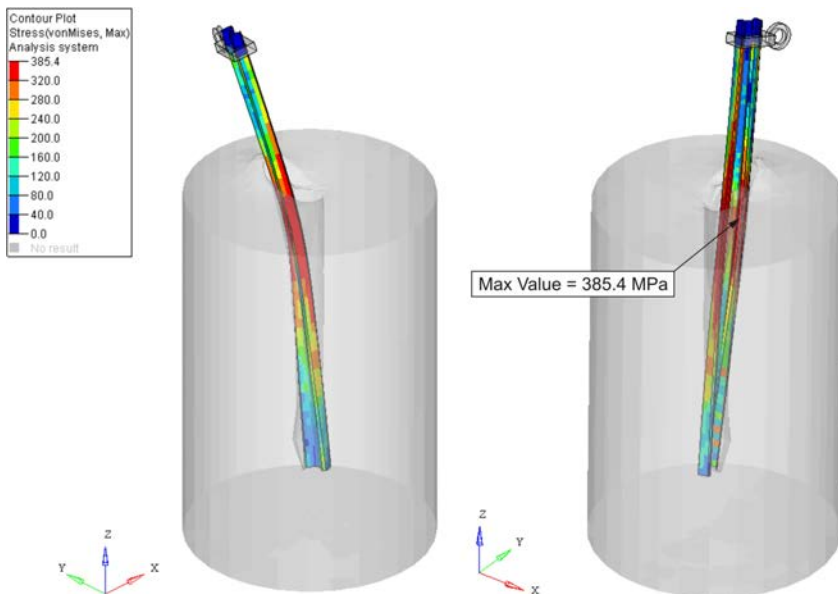


FIG. 17. Effective stress contour map for deformed SIGMA-100 post embedded in soil S, with displacement $s_1 = 300$ mm.

5.2. Solid finite elements with full integration

The simulations using solid finite elements with full integration were performed for control purposes. Figure 18 shows the $F(s_1)$ simulation curves using finite elements with full integration (ELFORM_2), for cohesive soils S, M, and H, against the background of the experimental curve.

In the case of soil S, for which the best compliance with the experimental result was obtained, the calculations were discontinued at displacement $s_1 = 338.7$ mm, due to the occurrence of a negative volume of finite elements. The $F(s_1)$ curves shown in Fig. 18 correspond well with the results shown in Fig. 11. The results confirm the reduced integration preference.

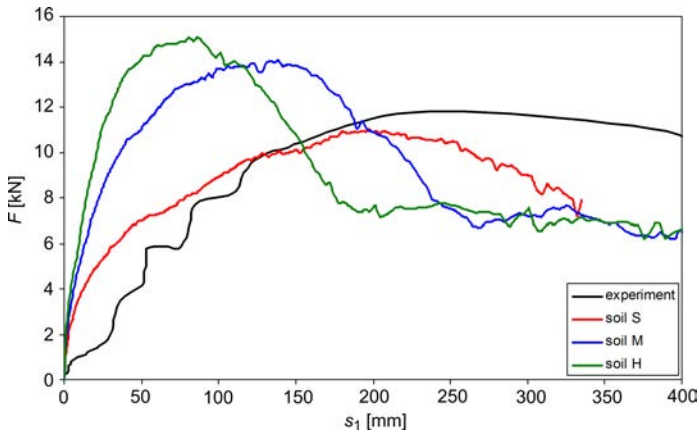


FIG. 18. $F(s_1)$ curves for soils S, M, and H, against background of experimental curve (full integration).

6. CONCLUSIONS

In the study, the problem of material modelling of the road side soil has been solved analytically. Due to the fact that the location of a given barrier is not known, values of elastic-plastic soil parameters were determined for the mean values of the input soil parameters taken from the references. The calculations were made for soft, medium and hard plastic cohesive soils.

The parameters of the soil material model *MAT_005_SOIL_AND_FOAM were determined for dehydrated soil, because such conditions are present in the ground of roadsides. The determination of these constants is independent of the validation experimental test. Comparison of the simulation results with the validation experimental test results allowed to verify the displacements and deformations of the upper part of the post and to assess the condition of the soil on the testing ground where the test was performed. This assessment is a hy-

pothesis. In order to prove it fully, identification tests of irrigated soil would be necessary.

The final conclusions are as follows:

- A new analytical algorithm for determining the elastoplastic parameters for plastic cohesive soils, corresponding to *MAT_005_SOIL_AND_FOAM material model available LS-Dyna FE code, can be applied for specific dehydrated road side soil identified experimentally in the scope of the material constants E , G , ν , $c\varphi$.
- In the case of an unknown location of the road side, a set of elastoplastic coefficients specified in Table 7 is recommended. This set corresponds to MAT_005_SOIL_AND_FOAM material model and dehydrated medium plastic cohesive soil with average values of the material constants E , G , ν , $c\varphi$.
- The numerical modelling methodology of the post-soil subsystem, developed in the study, can be applied to numerical modelling and simulation of crash tests of road safety barriers.
- The experimental test, i.e. a Sigma-100 steel post partly embedded in the soil and subjected to a static flexural-torsional test using a horizontal tensioned rope, it is not fully useful for the validation of numerical modelling and simulation of post-soil interaction, due to the lack of full soil dehydration. Nevertheless, partial validation of the displacement-controlled excitation was possible and included the displacements and deformation of the post.
- Comparison of the simulation results with the experiment, in the form of graphs of the rope tension vs. displacement of the upper measurement point on the post and in the form of deformation of the post-soil system, proved that the experiment was conducted on the post embedded in partly irrigated soft plastic cohesive soil.

ACKNOWLEDGEMENTS

The study was supported by a block grant (year 2017) from Ministry of Science and Higher Education, Poland. Translation of the article was provided by Mrs. Christine Frank-Szarecka, Canada.

REFERENCES

1. WU W., THOMSON R., *A study of the interaction between a guardrail post and soil during quasi-static and dynamic loading*, International Journal of Impact Engineering, **34**: 883–898, 2007.

2. GABAUER D.J., KUSANO K.D., MARZOUGUI D., OPIELA K., HARGRAVE M., GABLER H.C., *Pendulum testing as a means of assessing the crash performance of longitudinal barrier with minor damage*, International Journal of Impact Engineering, **37**: 1121–1137, 2010.
3. ROHDE J., ROSSON B., SMITH R., *Instrumentation for determination of guardrail-soil interaction*, Transportation Research Record, **144**: 109–115, 1996.
4. PLAXICO C., PATZNER G., RAY M., *Finite-element modeling of guardrail timber posts and the post-soil interaction*, Transportation Research Record, **146**: 139–146, 1998.
5. SHEIKH N.M., ABU-ODEH A.Y., BLIGH R.P., *Finite element modeling and validation of guardrail steel post deflecting in soil at varying embedment depths*, Proc. of 11th International LS-DYNA Users Conference, pp. 11–32, 2011.
6. ATAHAN A.O., *Finite Element Simulation of a Strong-Post W-Beam Guardrail System*, Simulation, **78**: 587–599, 2002.
7. NOH M.-H., LEE S.-Y., *Construction tolerance effects of reinforced posts on crash performances of an open-type guardrail system*, Thin-Walled Structures, **120**: 138–152, 2017.
8. REN Z., VESENJAK M., *Computational and experimental crash analysis of the road safety barrier*, Engineering Failure Analysis, **12**: 963–973, 2005.
9. BOROVINSEK M., VESENJAK M., ULBIN M., REN Z., *Simulating the impact of a truck on a road-safety barrier*, Journal of Mechanical Engineering, **52**: 101–111, 2006.
10. BOROVINSEK M., VESENJAK M., ULBIN M., REN Z., *Simulation of crash tests for high containment levels of road safety barriers*, Engineering Failure Analysis, **14**: 1711–1718, 2007.
11. GUTOWSKI M., PALTA E., FANG H., *Crash analysis and evaluation of vehicular impacts on W-beam guardrails placed behind curbs using finite element simulations*, Advances in Engineering Software, **114**: 85–97, 2017.
12. KLASZTORNY M., NY CZ D.B., SZURGOTT P., *Modelling and simulation of crash tests of N2-W4-A category safety road barrier in horizontal concave arc*, International Journal of Crashworthiness, **21**(6): 644–659, 2016.
13. KLASZTORNY M., ZIELONKA K., NY CZ D.B., POSUNIAK P., ROMANOWSKI R.K., *Experimental validation of simulated TB32 crash tests SP-05/2 barrier on horizontal concave arc without and with composite overlay*, Archives of Civil and Mechanical Engineering, **18**(2): 339–355, 2018.
14. QIAN G., MASSENZIO M., ICHCHOU M., *Development of a W-beam guardrail crashing model by considering the deformations of components*, ICMCE'16 Proc. 5th Int. Conf. on Mechatronics and Control Engineering, pp. 42–46, December 14–17, 2016, Venice, Italy, <http://dx.doi.org/10.1145/3036932.3036939>.
15. HARRIS D.W., *Computer material models for soils, rock, and concrete using FLAC and DYNA*, Technical Report DSO-06-01, Denver, Colorado: Bureau of Reclamation, Technical Service Center, Materials Engineering and Research Laboratory, 2006.
16. HALLQUIST J.O., *LS-DYNA Theory Manual*, Livermore, CA, USA, Livermore Software Technology Corp., 2006.
17. THOMAS M.A., CHITTY D.E., GILDEA M.L., T'KINDT C.M., *Constitutive soil properties for Cuddeback Lake, California and Carson Sink, Nevada*, NASA/CR-2008-215345, Hampton, Virginia, NASA Langley Research Center, 2008.

18. FASANELLA E.L., LYLE K.H., JACKSON K.E., *Developing soil models for dynamic impact simulations*, NASA Langley Research Center, in support of the Subsonic Rotary Wing (SRW) Aeronautics Program and the Orion Landing System (LS) Advanced Development Program (ADP), <https://ntrs.nasa.gov/archive/nasa/casi.ntrs.nasa.gov/20090022374.pdf> [accessed November 2, 2017].
19. PALMER T., HONKEN B., CHOU C., *Rollover simulation for vehicles using deformable road surface*, 12th International LS-Dyna Users Conference, <http://www.dynalook.com/international-conf-2012/automotive01-a.pdf> [accessed November 2, 2017].
20. HALLQUIST J.O., *LS-DYNA Keyword User's Manual*, Livermore, CA, USA, Livermore Software Technology Corp., 2007.
21. *System N2 W4 (SP-05/2)*, Bochnia, Poland, Stalprodukt Co., 2011.
22. Hourglass (HG) Modes, Livermore, CA, USA, Livermore Software Technology Corp., <http://ftp.lstc.com/anonymous/outgoing/jday/hourglass.pdf> [accessed April 7, 2014].
23. CALA M., *Stresses and strains* [in Polish], Department of Geomechanics, Civil Engineering and Geotechnics, Academia of Mining and Metallurgy, Cracow, Poland, http://home.agh.edu.pl/~cala/prezentacje/3wyklad_ZG.pdf [accessed July 15, 2017].
24. CALA M., *Soil shear strength*, Department of Geomechanics [in Polish], Civil Engineering and Geotechnics, Academia of Mining and Metallurgy, Cracow, Poland, http://home.agh.edu.pl/~cala/prezentacje/6wyklad_ZG.pdf [accessed July 15, 2017].
25. WILUN Z., *Outline of geotechnics* [in Polish], WKL Press, Warsaw, 1982.

Received February 24, 2019; accepted version June 12, 2019.

Published on Creative Common licence CC BY-SA 4.0

